ADVANCED MATERIALS
www.advmat.de

Versatile Mesoporous Microblocks Prepared by Pattern-Induced Cracking of Colloidal Films

Yunchan Lee, Min-Gi Jo, Jaekyoung Kim, Ji Hoon Kim, Jae Jung Kim, Kookheon Char, and Hyunsik Yoon**

Mesoporous microparticles have the potential to be used in various fields, such as energy generation, sensing, and the environmental field. Recently, the process of making homogeneous microparticles in an economical and environmentally friendly way has gained much attention. Herein, rectangular mesoporous microblocks of various designs are produced by manipulating the fragmentation of colloidal films consisting of micropyramids while controlling the notch angles of pyramidal edges. During calcination of the colloidal films, cracks are generated in the valleys of micropyramids acting as notches, and the angle of notches can be controlled by the prepattern underneath the micropyramids. By changing the location of notches with sharp angles, the shape of microblocks can be controlled with excellent uniformity. After detaching the microblocks from substrates, mesoporous microparticles of various sizes with multiple functions are easily produced. This study demonstrates anti-counterfeiting functions by encoding the rotation angles of rectangular microblocks of various sizes. In addition, the mesoporous microparticles can be utilized for separating desired chemicals mixed with chemicals of different charges. The method of fabricating size-tunable functionalized mesoporous microblocks can be a platform technology to prepare special films and catalysts and for environmental applications.

1. Introduction

As environmental problems have emerged in past decades, the development of sustainable materials for energy and the environment has become a global issue. Mesoporous supraparticles, which have a 3D structure through assembly of nanoparticles (NPs), have attracted great attention as sustainable materials because they can utilize the NP functionality as well as structural features.[1–6] They have potential uses in various fields, such as catalysis,[7–9] energy conversion,[6,10,11] environmental purification,[12–14] biomedical applications[15] and smart communication.[16–18] To fabricate supraparticles of a uniform size, spray-drying process,[15,19] self-assembly with an emulsion,[20,21] or use of microfluidic devices[22,23] were suggested. These solvent-based methods are suitable for mass production; however, they require additional stabilizers or emulsifiers and entail waste problems after processing. Recently, the method of drying colloidal microdroplets on liquid-repellent surfaces was carried out to overcome these challenges.[24,25] This method produced large-scale spherical mesoporous supraparticles, and an advanced method to control the shape of the supraparticles was also suggested by tuning colloidal interactions[26] or contact lines[27] during the drying process. Despite these efforts,

Y. Lee, H. Yoon
Institute of Energy and Environment System
Seoul National University of Science and Technology
Seoul 01811, Republic of Korea
E-mail: hsyoon@seoultech.ac.kr

Y. Lee, K. Char
The National Creative Research Initiative Center for Intelligent Hybrids
The World Class University Program for Chemical Convergence for Energy and Environment
School of Chemical and Biological Engineering
Seoul National University
Seoul 08826, Republic of Korea
E-mail: khchar@snu.ac.kr

M.-G. Jo, H. Yoon
Department of Chemical and Biomolecular Engineering
Seoul National University of Science and Technology
Seoul 01811, Republic of Korea

J. Kim, H. Yoon
Department of Energy and Chemical Engineering
Seoul National University of Science and Technology
Seoul 01811, Republic of Korea

J. H. Kim
School of Chemical and Biological Engineering
Seoul National University
Seoul 08826, Republic of Korea

J. J. Kim
Department of Chemical Engineering
Hongik University
Seoul 04066, Republic of Korea

The ORCID identification number(s) for the author(s) of this article can be found under https://doi.org/10.1002/adma.202300952

DOI: 10.1002/adma.202300952

the shape of the supraparticles, such as a disk or a hemisphere, should be transformed from the spherical base.

Harnessing crack generation in colloidal films can be a method to fabricate supraparticles with good uniformity. Previously, a concept for producing microparticles through crack-induced isolation of microshapes in colloidal films was proposed.[28] Generally, tensile stresses can be generated by volume shrinkage, and irregular cracks can be formed during drying of solvents or organic additives in colloidal films.[29,30] By imprinting micropyramidal shapes on wet colloidal films, cracks could be generated in the notches, and homogeneous pyramidal fragments could be obtained.[28,31] This process has the advantages of producing microparticles economically and environmentally because it can avoid any additional chemicals, such as solvents, stabilizers, and emulsifiers. However, in the previous studies,[28,31] the controllability of sizes and functions in the production of micro-scale fragments was limited. In this study, we proposed a new approach to prepare versatile mesoporous micro-scale blocks of various shapes and sizes by specifying the position of notches for crack generation. Colloidal films with pyramidal shapes regularly cracked at the desired position under the influence of the patterns under the colloidal films. By combining notch effects and underlying patterns, we successfully fabricated rectangular mesoporous micro-scale blocks and investigated the mechanism of control in crack generation. After detachment of microblocks from substrates by tapping or sonication, we obtained regular microblocks of various sizes. Mesoporous microblocks can be individually adjusted to have different surface areas as well as various functionalities. By utilizing these advantages, we prepared colored microblocks by inserting photoluminescent quantum dots into the mesoporous microblocks. We demonstrated an array of microblocks of different colors (red, green, and blue) at desired positions by synchronizing the sizes of microblocks and microwells in a substrate. Each microblock trapped in a well has a specific rotation angle, and we fabricated an anti-counterfeiting film with a high encoding capacity even with a smaller array by utilizing the rotation angle as a new encoding parameter. Furthermore, for environmental applications, we separated two different chemicals by absorbing them onto microblocks with different charges and sizes. After separation of microblocks of different sizes, we could selectively obtain microblocks that absorbed the desired chemicals and eliminate undesired chemicals through the photocatalytic effect of TiO_2. Finally, the desired chemicals could be collected by dissociation of the chemicals from the microblocks. The concept of the fabrication of microblocks of different shapes, sizes and functionalities by cracking colloidal films suggests a simple, economic and environmentally friendly process. The versatile mesoporous TiO_2 blocks can open doors for application in scientific research and industrial fields.

2. Results and Discussion

2.1. Effect of Prepattern on Crack Formation

We developed a method to isolate a colloidal film into uniform fragments by controlling the positions of cracks. **Figure 1**a shows a schematic illustration of the production of mesoporous rectangular microblocks consisting of TiO_2 NPs by manipulating cracks. Prepatterned substrates (lines and square pillars) were prepared by a soft imprinting method on a wet TiO_2 paste, followed by soft annealing (at 60 °C) to remove residual solvent (Figure S1, Supporting Information; the detailed procedure can be seen elsewhere (refs. [28,31])). Then, we coated a wet TiO_2 paste again on the prepatterns by the doctor blading method and placed a poly(dimethylsiloxane) (PDMS) mold with inverted pyramidal shapes on the paste. Then, the wet paste moved into the voids in the PDMS mold via the capillary force. After soft annealing (at 60 °C), we detached the PDMS mold from the solidified TiO_2 films with pyramidal shapes on the surface. Then, we calcinated the films at high temperature (500 °C) to crack the films through evaporation of all organic compounds in the colloidal films. The width (W) and spacing (S) of the prepattern were designed to be multiples of the period of a unit micropyramid (Figure 1b). The dimensions of the unit micropyramid were 30 μm in period and 45° in inclination angle. After soft molding, notches were formed at the edges of pyramids, and crack generation occurred during the calcination step. We note that every notch with a relatively thin thickness (below ≈12 μm) can be an initiation tip; however, crack generation can be random when the thickness of the colloidal films is >20 μm.[31] In this paper, we conducted the process with a film thickness greater than 20 μm, and cracks were generated in a random way without a prepattern (Figure 1c). When we generated cracks in colloidal films coated on line patterns, cracks could be generated along all vertical lines, and horizontal cracks were randomly generated (Figure 1d). When we generated cracks in films on square pillars, as shown in Figure 1e, cracks were regularly generated between pillars through the combination of notch effects and prepatterns.

2.2. Mechanism of Controlling the Crack Position by Prepattern

The illustration in **Figure 2**a shows the mechanism of controlling cracks through the combination of notch effects and prepatterns. The width and spacing of prepatterns (lines and pillars) were 30 μm, which is identical to the period of unit pyramids. The notches (edges of micropyramids) were alternately imprinted on pillars (blue arrow) and between pillars (red arrow) when the inverted pyramidal molds were aligned on TiO_2 wet paste coated on prepatterns. After coating a TiO_2 wet paste over a solidified prepattern by the doctor blading method, the mass of the wet paste was different on and between pillars. Because the mass of the wet paste between pillars was more than that on pillars, the volume shrinkage during the first annealing process (60 °C) of the film between pillars was higher than that of the film on pillars. Interestingly, the difference in volume shrinkage caused a change in the notch angles, from θ to α (on pillar) and β (between pillar), as shown in the middle image of Figure 2a. After the calcination step, cracks were generated only at the notches between pillars, which had sharper notch angles.

To determine the locations of notches and prepatterns, we used 20 nm TiO_2 NPs for prepatterns (lines and pillars) and a mixture of TiO_2 NPs 20 and 250 nm in diameter (1:1 weight mixture) for micropyramids. Then, we clearly found the boundary of the prepattern as well as the positions of the notches by scanning electron microscopy (SEM) (Figure 2b–d). The cross-sectional SEM images in Figure 2b show that the paste of the 1:1 NP mixture was uniformly coated and formed notches on

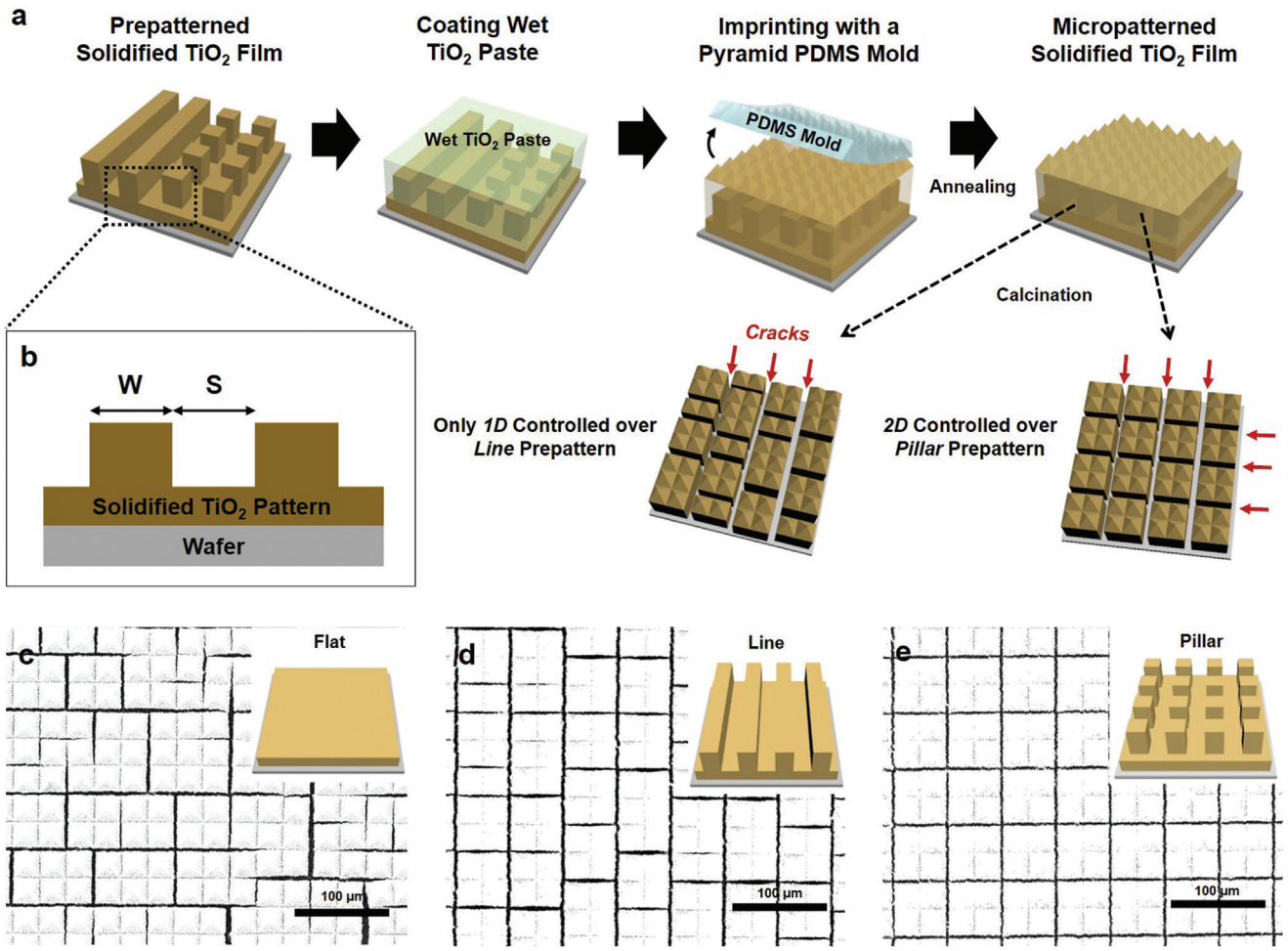

Figure 1. a) Schematic illustration of crack generation process in micropyramidal colloidal films coated on prepatterned substrates. b) Definition of the width (W) and spacing (S) of prepatterns. c–e) SEM images of cracked micropyramidal films on different prepattern geometries: c) flat surfaces, d) line patterns, and e) pillar patterns.

the flat 20 nm NP film. Therefore, the volume shrinkage occurred uniformly during the annealing process, maintaining the direction of the pyramid vertices as straight up (yellow arrows in Figure 2b). The notch angle (θ) was 92.5° ± 1.3° in every notch. When the wet paste was coated on pillar or line patterns, as shown in Figure 2c, the notch angle on pillars (α) was greater than that between pillars (β) due to the difference in the contraction of the wet paste during soft annealing (60 °C). After annealing, the directions of the pyramid vertices became slanted (yellow arrows in Figure 2c), and the notch angle on pillars (α) increased to 106.4° ± 2.8°, whereas the notch angle between pillars (β) decreased to 82.9° ± 1.9° (Figure 2c). After the calcination process, cracks were generated between pillars because the stress concentrated only at the sharper notches (Figure 2d). We further analyzed the angle change of notches with finite element method (FEM) simulations (Figure 2e,f). The simulation results showed that the angle of the notches on prepatterns was changed due to the difference in the amount of mass and volume shrinkages, and the notches between pillars became sharper than those on pillars, which was the same as in the experiment.

2.3. Control Various Size of Rectangular Microfragments

We further investigated the effect of the widths and spacings of pillars (or lines) on the selective crack generation, as shown in **Figure 3**. One or more notches were placed between the pillars depending on the dimensions of the prepattern, and the cracks propagated at relatively sharp notches. First, we fixed the width of the pillars to 30 μm (which is the same as the period of the unit pyramids) and changed the spacing between pillars. When the notches were positioned as shown in Figure 3a (spacing = 60 μm), one notch was between pillars, whereas two notches were near pillars. We compare the notch angles denoted α, β, and γ in Figure 3b, and the angle of the middle notch is sharper than that of the neighbors. Although the difference in notch angle is small (≈5 degrees), cracks were generated in the notches in the middle between pillars after calcination (Figure 3c). When the spacing was increased to 90 μm, three notches were positioned between the pillars (Figure 3d); however, the difference in the notch angles was reduced to less than one degree (Figure 3e). Therefore, cracks were generated at the γ position (red arrow in Figure 3f) as well as at other positions (γ and δ, yellow arrow in Figure 3f). This means

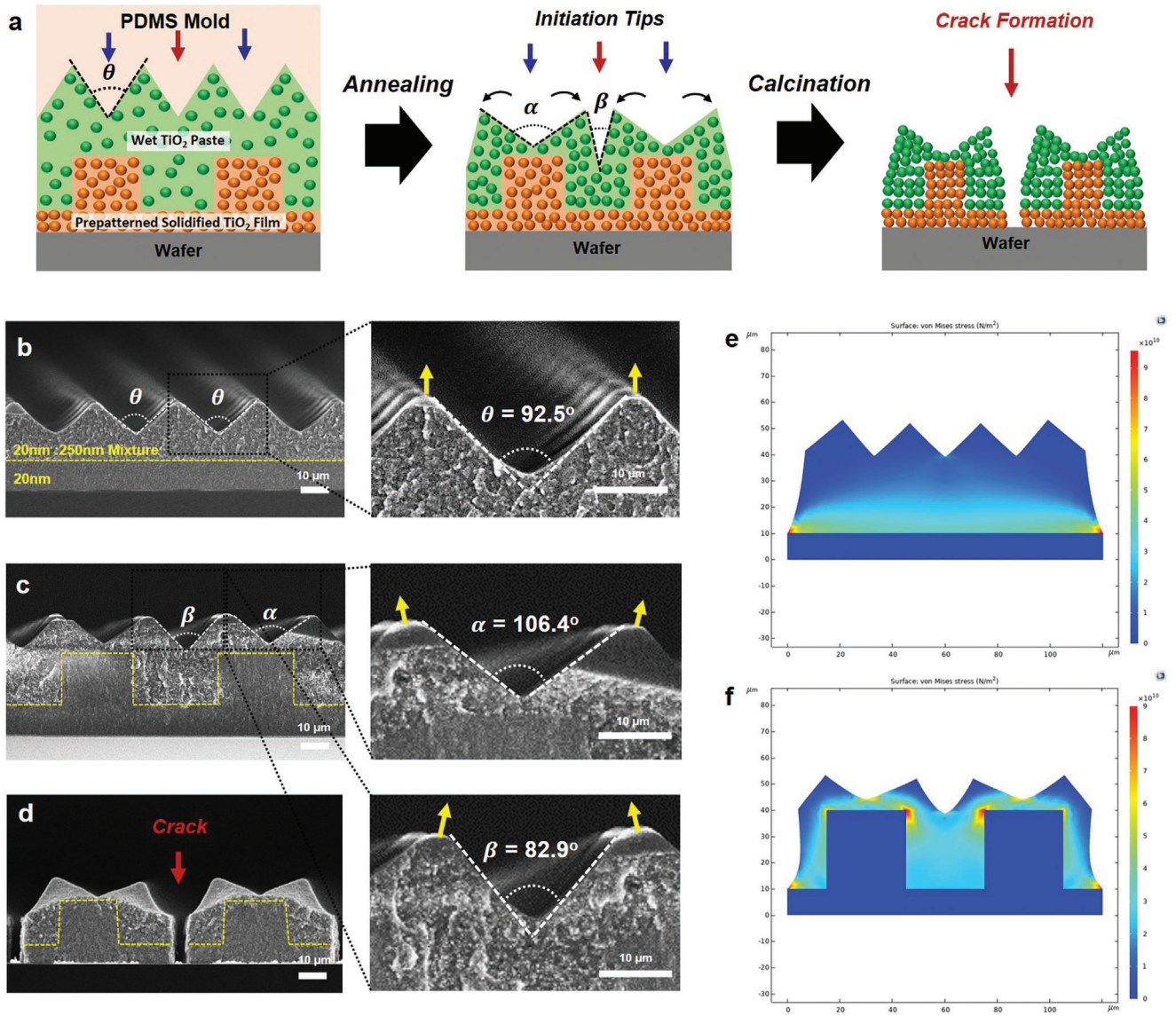

Figure 2. a) Schematic illustration of the change in the notch angles on and between pillars and cracked notch. b,c) Cross-sectional SEM images after annealing process (60 °C) when the micropyramidal patterns were imprinted on a flat substrate (b) and a pillar patterned substrate (c). The prepattern substrate was prepared from 20 nm TiO_2 paste, and pyramidal structures were prepared from a 1:1 (w/w) mixture of 20 nm and 250 nm TiO_2 pastes. The yellow dashed line indicates the boundary between the prepattern and pyramid pattern. d) Cross-sectional SEM images of crack propagation notches after the calcination process. e,f) FEM simulation results after volume shrinkage on a flat substrate (e) and a pillar patterned substrate (f).

that the spacing of the 30 μm width pillar pattern for selective crack generation was limited to 60 μm.

Then, we doubled the width of the pillars to 60 μm and investigated the angle differences by changing the spacings of the pillars. When the spacing was 30 μm, only one notch was located between pillars (Figure 3g). The angle difference between notches on pillars (α, γ) and notches between pillars (β) was ≈22° (Figure 3h). This higher difference can induce crack generation only between cracks, as shown in Figure 3i. When the spacing was 60 μm (Figure 3j), one notch was placed between pillars, and the notch angle between pillars (γ) was smaller than that of the neighbors (β,δ) (Figure 3k). Therefore, we could control the crack positions in regular ways to divide four pyramids (Figure 3l). When the spacing was 90 μm, three notches with small angle difference were placed between pillars, and cracks randomly propagated among the three notches. (Figure S2, Supporting Information)

Figure 3m shows a schematic to define the angle difference among middle and neighboring notches between pillars. We summarize the experimental results in Figure 3n,o. The notch angle difference compared to the neighbors was reduced when the spacing of the prepattern was increased. In our experiment, the crack generation position was controlled when the difference in notch angle compared to the neighboring notches was higher than 5 degrees (Figure 3n). Furthermore, increasing the width of the prepattern made fragments larger (Figure 3o; 90 μm width

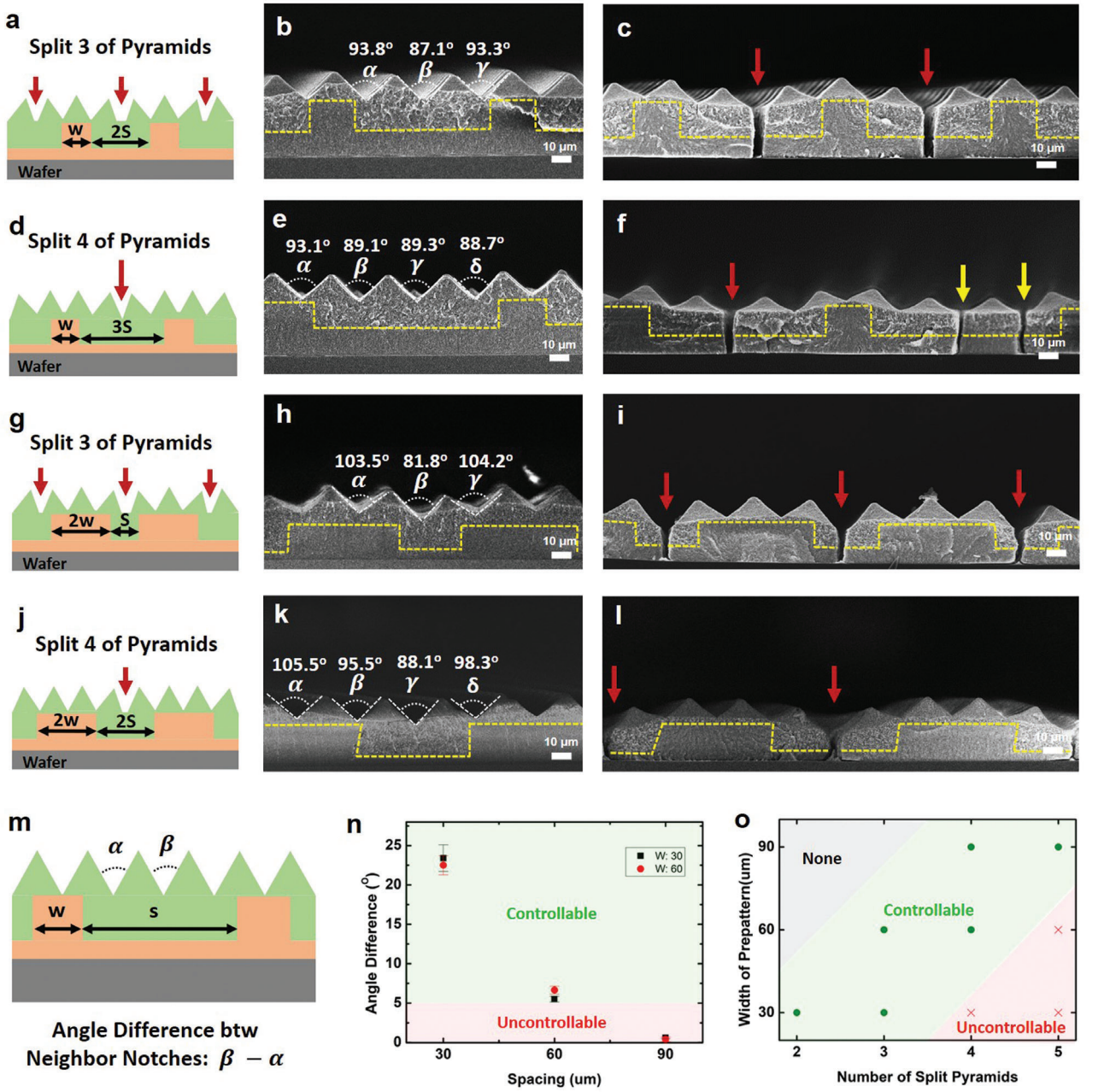

Figure 3. a) Schematic showing the positions of notches when micropyramids were located on the prepattern (width: 30 μm, spacing 60 μm). The red and yellow arrows indicate the desired and undesired positions of crack generation, respectively. b,c) SEM images of notch angles before calcination (b) and after calcination at 500 °C (c). d,g,j) Schemes showing the position of notches and prepatterns when the width is 30 μm and the spacing is 90 μm (d), when the width is 60 μm and the spacing is 30 μm (g), when the width is 60 μm and the spacing is 60 μm (j). e,h,k) SEM images before calcination when the width is 30 μm and the spacing is 90 μm (e), when the width is 60 μm and the spacing is 30 μm (h), when the width is 60 μm and the spacing is 60 μm (k). f,i,l) SEM images after calcination when the width is 30 μm and the spacing is 90 μm (f), when the width is 60 μm and the spacing is 30 μm (i), when the width is 60 μm and the spacing is 60 μm (l). m) Schematic of the crack width (W) and spacing (S) of the prepattern and notch angle difference between neighboring notches. n,o) Diagrams of the relationships between the geometric conditions and the controllability of crack generation (n) and between the number of pyramids in the fragments and the controllability of crack generation (o).

prepattern results in Figure S3, Supporting Information). We note that alignment between pyramid notches and prepatterns is important to split the exact number of pyramids because it determines the number of notches between pillars. For example, even when the condition for dividing three pyramids was satisfied (Figure 3a–c), the film was divided into two and one pyramids when the alignment was mismatched (Figure S4, Supporting Information). We checked the positions of pyramids imprinted on prepatterns by an optical microscope after using TiO_2 particles of different sizes in the pyramids and prepatterns, as discussed in

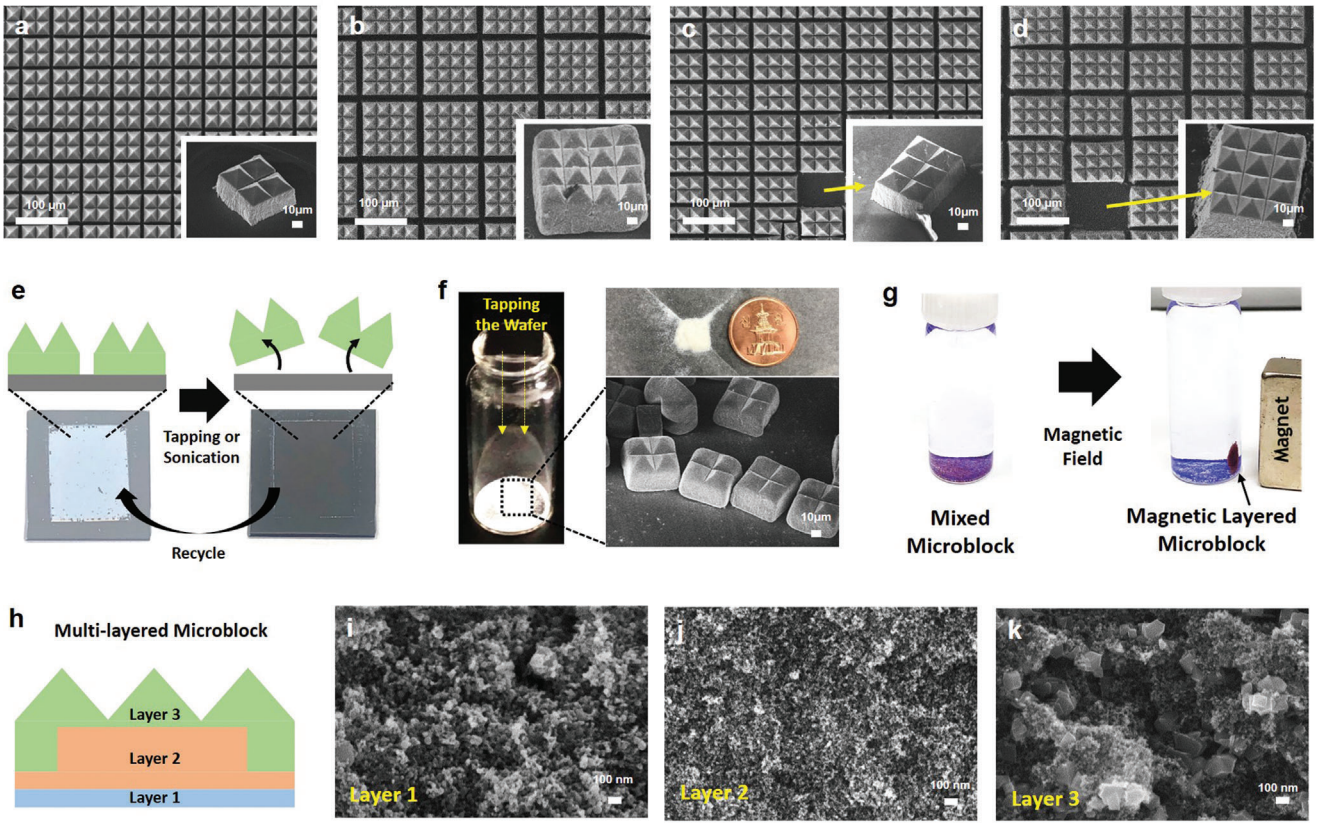

Figure 4. SEM images of cracked colloidal films of 2×2 (a) and 4×4 (b) pyramids for square shapes and 2×3 (c) and 3×4 (d) pyramids for rectangular shapes. The inset images show the mesoporous microblocks detached from the substrate. e) Scheme and photographs of detaching microblocks from the substrate by the tapping or sonication method. f) Image of mass-produced 2×2 microblock powder (0.5 g) collected in a vial. g) Photograph of mixed microblocks dispersed in water (left). Magnetic layered microblocks could be collected by applying a magnetic field (right). h) Scheme of multilayered microblocks consisting of different NPs. i–k) SEM images of magnetic NPs in layer 1 (i), ≈20 nm NPs in layer 2 (j), and the 1:1 mixture (wt%) of ≈20 and ≈250 nm NPs in layer 3 (k).

Figure 2. As shown in Figure S5 (Supporting Information), the prepattern (pillar or line) was relatively dark in the optical microscopy images (yellow dash), and both the prepattern and the pyramid notches were clearly observed after the annealing and calcination steps.

2.4. Fabrication of Versatile Microblocks with Various Sizes and Functionalities

We utilized the crack manipulation method on colloidal films to produce mesoporous microblocks of various sizes and functionalities. **Figure 4**a–d shows size-controlled square fragments of 2×2 (a) and 4×4 (b) and rectangular fragments of 2×3 (c) and 3×4 (d) after cracking. The inset images show the microblocks of each size after detachment from the substrate. To fabricate isotropic (for square microblocks) and anisotropic (for rectangular microblocks) microblocks, we designed the prepattern (pillar arrays) and summarize the relationship between the prepattern and microblock size in Table S1 (squares, Supporting Information) and Table S2 (rectangles, Supporting Information).

The microblocks were easily detached from the substrate by tapping or ultrasonication in ethanol. The picture in Figure 4e shows that the microblocks on the substrate were clearly detached after 3 s of sonication or tapping and that the wafer could be reused after detachment of the microblocks. We mass-produced microblocks of homogeneous sizes, as shown in Figure 4f. Figure S6 (Supporting Information) shows optical microscopy images of cracked colloidal films in a large area. Regardless of their sizes, the accuracy of crack generation to produce rectangular particles was over 90%. We note that there have been other methods utilizing crack generation with underlying patterns.[33] However, the uniformity and controllability were not good compared to our approach with the combination of V-shape notches and underlying patterns. In addition, taking advantage of our fabrication method, we prepared TiO_2 mesoporous microblocks with magnetic properties as well as different porosities. After the preparation of microblocks with magnetic properties, we could collect or separate specific size microblocks (Figure 4g). Figure 4h shows a schematic of microblocks fabricated with three different types of paste: layer 1 with TiO_2 (≈20 nm)/magnetic NP (Fe_2O_3) mixed paste (Figure 4i; energy-dispersive X-ray spectroscopy (EDS) analysis in Figure S7, Supporting Information), layer 2 with TiO_2 (≈20 nm) paste (Figure 4j) and layer 3 with TiO_2 (≈20 and ≈250 nm NP 1:1 wt% mixture) mixed NP paste (Figure 4k). Multilayered

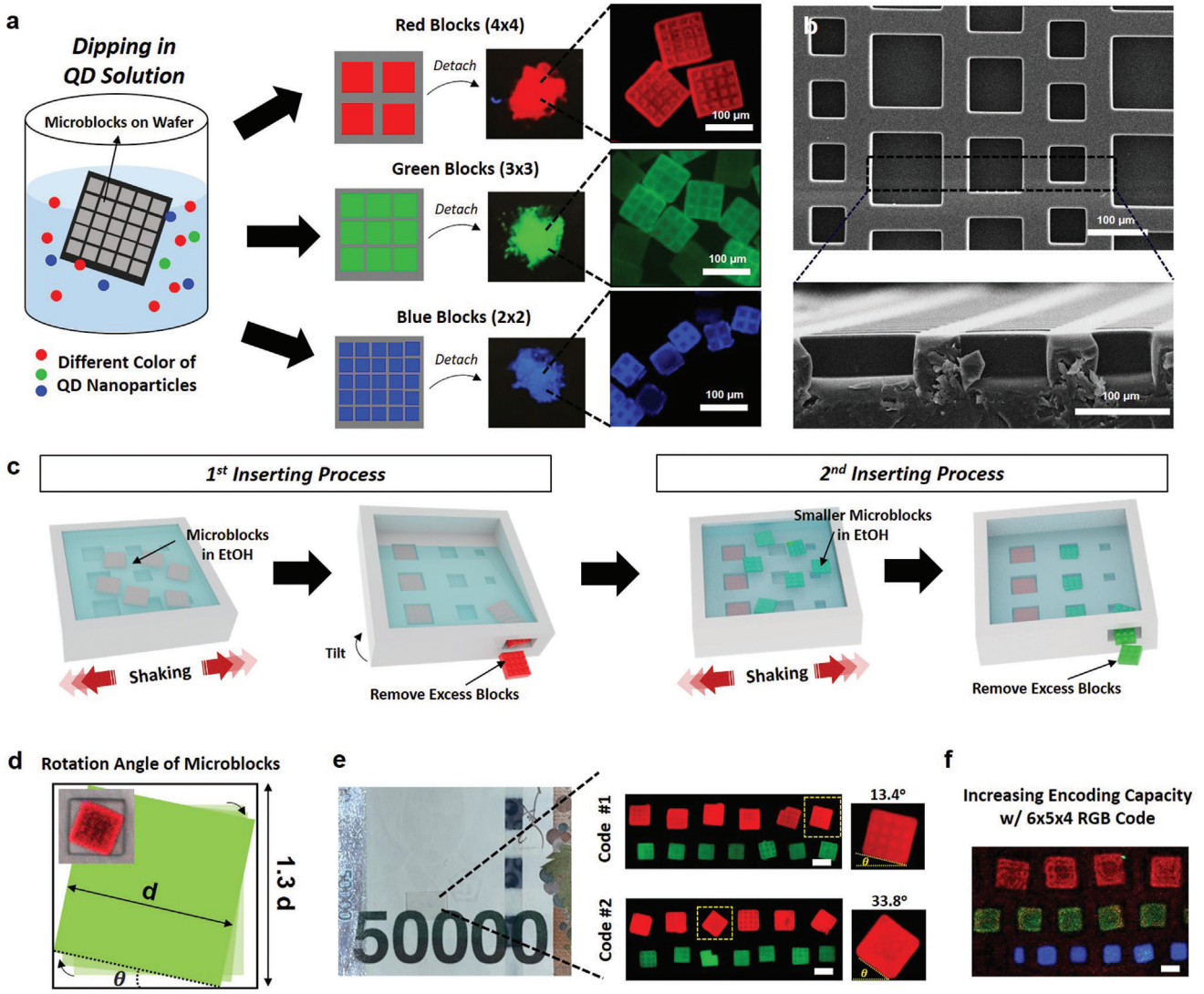

Figure 5. a) Scheme of the preparation process for colored microblocks. The photographs and fluorescence images show colored microblocks after insertion of QD NPs. b) SEM images of the microwell array for trapping microblocks. c) Schematic illustration of the process for trapping microblocks into microwells. d) Rotation angle of a microblock trapped in a microwell. The inset confocal microscopy image shows rotated microblock in this experiment. e) Encoded red and green microblocks trapped in two-distinct-sized 13-microwell array. The fluorescence images show that the colors of the arrayed blocks in code #1 and code #2 were the same; however, the rotation of each block was different. Scale bars: 100 μm. f) RGB blocks in three-distinct-sized 15-well array for enhancing the encoding capacity. Scale bars: 50 μm.

micro-scale blocks consisting of nanoparticles with different sizes and functions can have multiple functionalities, such as magnetism, color, charge, and photocatalytic effects. In this study, we produced multifunctional mesoporous rectangular particles with controlled sizes and good uniformity by controlling the positions of the shaped notches for crack generation.

2.5. Microblocks for Anti-Counterfeit Film

Mesoporous TiO_2 microblocks of controlled sizes can be utilized in various applications by harnessing the mesoporosity, rectangular features and photocatalytic effects. First, we demonstrated the fabrication of optically encoded films by using trapped microblocks of different colors and sizes. **Figure 5**a shows the process of insertion of quantum dots of different colors into microblocks of different sizes. After calcination of colloidal films, we dipped the cracked films in toluene solutions with dispersed photoluminescent quantum dots (QDs). After the insertion of QDs within the mesoporous microblocks, we could fabricate microblocks with colors provided by QDs. Since the mesoporous microblocks were composed of ≈20 nm (or ≈250 nm) NPs, QDs with sizes less than 10 nm could be successfully inserted into the microblocks, as shown in a confocal microscopy image (Figure S8, Supporting Information). We detached colored microblocks on the gram scale by sonication, as shown in Figure 5a. To trap the microblocks, we prepared a film with a microwell array of three different sizes (Figure 5b). The sizes of wells were

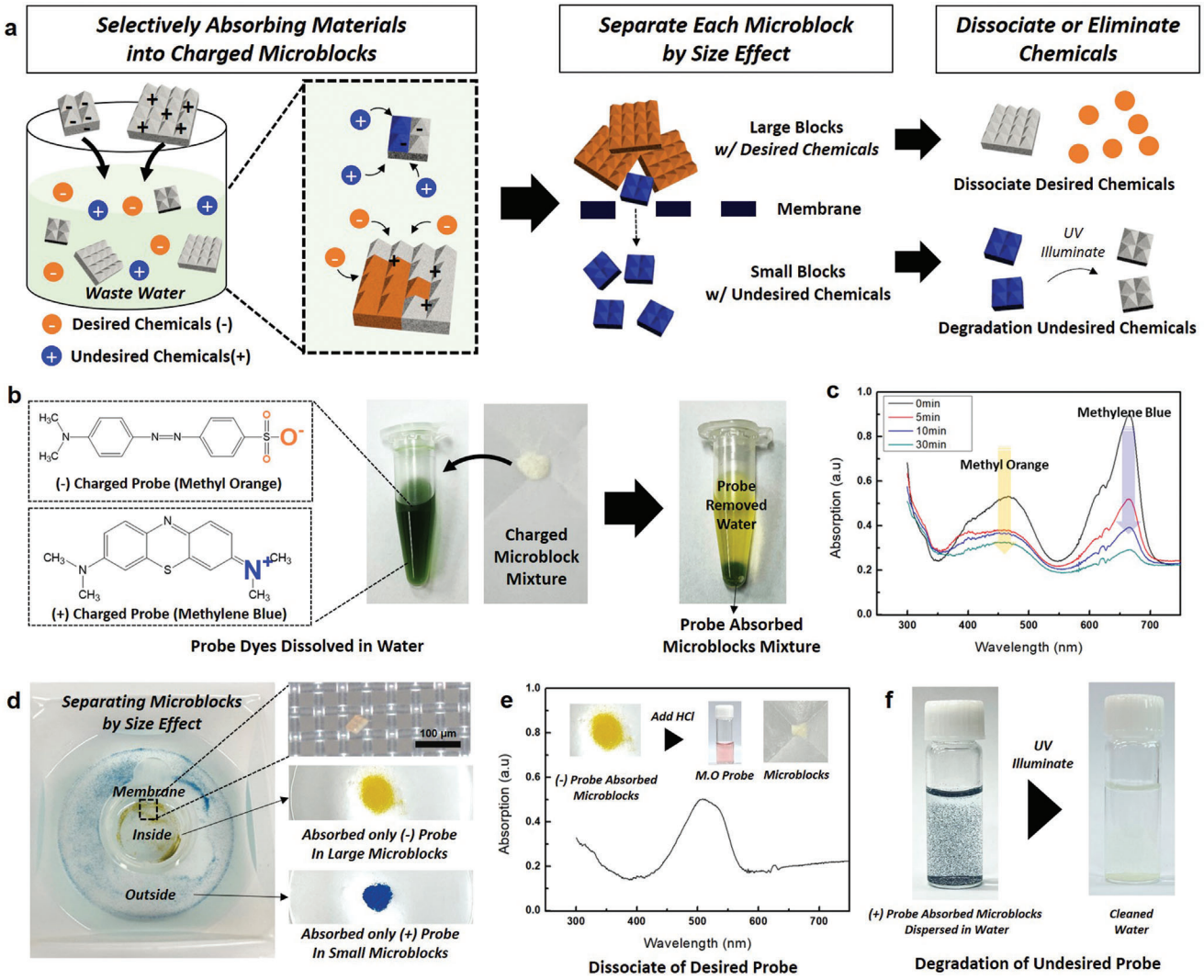

Figure 6. a) Schematic illustration of selective absorption and separation of charged probes via electrostatic interactions with charged microblocks. b) Picture of removing mixed dyes dispersed in water by using mixtures of microblocks with different charges. c) UV–vis absorption spectra of the solution after absorption probe dyes by charged mesoporous microblocks. d) Photograph after the separation of mixed microblocks by membrane grid. e) UV–vis absorption spectra of the solution with desired probe (MO) after dissociation from charged microblocks. The inset photos show the dissociated dye and charged microblocks. f) Photograph showing elimination of the undesired probe (MB) through the photocatalytic effect under UV illumination.

designed to be ≈1.4 times larger than microblocks designated to be trapped. The schematic illustration in Figure 5c depicts the process of arrangement of microblocks into the microwell arrays. The largest microblocks (4×4 red blocks) were inserted into size-matched wells after gently shaking them in ethanol. The rest of the blocks were eliminated by opening the hole on the bottom side, and the red-colored array was successfully generated. We repeated this process with green, medium-sized (3×3) blocks, obtaining a red/green-colored array. Next, blue, small-sized (2×2) blocks were arranged, generating a three-colored RGB array. Each microblock had a unique rotation angle in the microwell due to the large hole size, and the square-shaped microblocks made measurement of the rotation angle (θ) easy (Figure 5d). The inset confocal microscopy image in Figure 5d showed rotated microblocks in the microwells. Geometrically, the microblocks rotated clockwise or anticlockwise up to ≈35° ($\cos\theta + \sin\theta = 1.4$), and one microblock could generate 351 cases (setting the scale of the minimum variation in the angle to 0.2°, details in Note 1, Supporting Information) of the rotation angle. This means that the assembly of microblocks in two-distinct-sized 13 microwells has an encoding capacity of ≈10^{37} ($C^S \times (S \times m)^B$) where C is the number of color choice, S is the number of size choice, B is the number of wells, and m is the number of rotations angles). Compared to previous research,[32] we dramatically increased the encoding capacity even with a smaller array by utilizing the rotation angle as the new encoding parameter in addition to the color and size. This concept could be applied to anti-counterfeiting of bills (Figure 5e). The rotation angles of codes #1 and #2 were completely different (Figure S9, Supporting Information). We further increased the encoding capacity to ≈10^{46} by changing the number of blocks and the array, such as the three-distinct-sized 15 RGB array in Figure 5f.

2.6. Microblocks for Selectively Separating Chemical

Mesoporous microblocks with different sizes can be used for separating desired chemicals mixed with undesired chemicals. **Figure 6**a shows the experimental procedure to separate the desired chemicals with mesoporous microblocks. After absorption of two chemicals by mesoporous microblocks with two different charges, as a proof of concept, we separated the blocks by size, detached the desired chemicals from the mesoporous microblocks and eliminated the undesired chemicals through the photocatalytic effect of TiO_2. Figure 6b shows that size-controlled microblocks were dipped into a solution with mixed desired and undesired chemicals. Negatively charged small microblocks (2×2) and positively charged large microblocks (4×4) were prepared by coating with poly(sodium 4-styrenesulfonate) (PSS) and poly(diallyldimethylammonium chloride) (PDAC), and the charged state of each charged microblock was −15.2 mV ± 6.3 and 11.3 mV ± 4.5, respectively. The zeta potential of charged microblocks was measured by an electrophoretic light scattering spectrophotometer (ELS-8000). Methyl orange (MO) dye (negative charge) was used as a probe of a desired chemical for selective separation, and methylene blue (MB) dye (positive charge) was used as a probe of an undesired chemical for selective elimination. Before the insertion of microblocks, the color of the solution was green, and it changed to yellow after the absorption of chemicals on charged microblocks for 30 min (Figure 6b). The time-dependent UV–vis adsorption spectra in Figure 6c indicate that MB and MO were gradually removed in 30 min. After the absorption process, the mixed microblocks were completely separated by the size effect through a membrane strainer (70 µm grid size), and the microblocks had selectively absorbed the charge-matched probes via electrostatic interactions (Figure 6d). The pure MO probe, the desired chemical, was successfully obtained after dissociation from microblocks under low pH conditions (Figure 6e). The microblocks still maintained the charge property, and they could be reused after the dissociation process. In contrast, the MB probe, an undesired chemical, was completely eliminated after illumination with UV for 30 min through the photocatalytic effect of TiO_2 microblocks (Figure 6f). This process proposes the concept of attaching functional groups to microblocks of various sizes to selectively absorb different materials and collect specific chemicals after dissociating the adsorbed materials or eliminate chemicals through particle separation.

3. Conclusion

We have proposed mass production of versatile and shape-controlled microblocks by manipulating cracks on colloidal films. We generated cracks in the colloidal films with pyramid arrays coated on designed prepatterns. We harnessed the change in notch angles on prepatterns and controlled the crack positions by differentiating the notch angles. After cracking colloidal films into various shapes, we detached the cracked fragments from the substrates and obtained versatile mesoporous microblocks. The microblocks could have various functionalities, such as magnetism, color, charge, and the photocatalytic effect. We conceptually demonstrated the preparation of anti-counterfeiting films by inserting colored microblocks randomly rotated in microwells, the separation of desired chemicals by using different electrostatic interactions with microblocks, and the elimination of undesired chemicals by the photocatalytic effect after separation. Compared to other methods used to produce microparticles, such as microfluidic and spray-drying approaches,[15,19,22,23] the proposed method has advantages such as excellent control of sizes and shapes of particles with multiple functions and good uniformity. Environmentally friendly methods of producing multifunctional versatile mesoporous microscale fragments can be used in various fields, such as catalytic processes, biomedical engineering, energy, and display devices.

4. Experimental Section

Tuning Porosity and Magnetic Property of TiO_2 Paste: TiO_2 colloidal pastes composed of TiO_2 NPs (20 nm, 250 nm) were purchased from Dyesol (DSL 18NR-T, WER2-O). 1 g of each 20 nm and 250 nm paste was mixed in a vial and sonicated for 1 h after adding 0.2 ml of ethanol. After sonication, the added ethanol was completely removed by drying gently with an air gun, and a homogeneous mixture of 20 nm and 250 nm pastes was prepared. The magnetic NP mixture paste was prepared by mixing 8 wt% magnetic NPs (Fe_2O_3) into the 20 nm paste, followed by sonication and vortex for 1 h.

Preparation of Colored and Charged Microblocks: Red and green QDs were purchased from PlasmaChem, and blue QDs were synthesized. QDs were dissolved in toluene, and the wafer with microblocks was dipped in the QD solution for 5 min and washed with ethanol. The wafer was sonicated in vial with ethanol for 3 s, and colored microblocks were obtained. The positively charged polymer solution (poly(diallyldimethylammonium chloride) (PDAC) solution, Mw < 100 000, 35 wt% in H_2O) and negatively charged polymer solution (poly(sodium 4-styrenesulfonate) (PSS) solution, Mw ≈70 000, 30 wt% in H_2O) were purchased from Sigma–Aldrich. The wafer with microblocks was dipped in each solution for 10 min and washed with deionized water. The wafer was sonicated in vial with water for 3 s and completely dried in oven. Then, the charged microblocks were obtained.

Fabrication of Anti-Counterfeiting Film: The positive microwell array poly(dimethylsiloxane) (PDMS) mold was prepared from PUA 301 (MC-Net Co., Ltd., South Korea)) replicated from a silicon master. The curable materials (NOA 81) were placed on the PET film and stamped with PDMS mold followed by photo (365 nm light) curing for 5 min. A wall was made around the film to trap ethanol, and the bottom side of the wall was designed to be openable for removal of ethanol. The colored microblocks were dispersed in ethanol and spread into the microwell film, followed by gentle shaking. The microblocks were inserted into the size-matched holes, and the remaining microblocks were removed by tilting the film and opening the bottom wall with squeezing of the ethanol. After drying the films at 60 °C for 10 min, we coated the film with a UV-curable adhesive (10 wt% PUA 301 in ethanol) followed by UV illumination for 10 min after drying ethanol completely to fix the microblocks. This process was repeated by changing the size of the microblocks and obtained an anti-counterfeiting film after cutting off the wall at the end of the process.

Selectively Separation of Dyes with Different Charges: Each aqueous methylene blue (MB) and methyl orange (MO) solution was prepared at a dye concentration of 0.2 mg mL^{-1} and mixed them equal volume ratio to prepare mixed solution. Then, 4 mg of microblock mixtures were added to the 1 mL of mixed solution and collected them after 30 min. The microblock mixtures were washed with ethanol and placed in a membrane kit (Falcon, Cell Strainers) followed by shaking in deionized water to separate them. The separated microblocks dispersed in water to dissociate and degrade the probe dyes. The MO probe dye was dissociated from microblocks after adding 20 µL of 6 N hydrochloric acid solution. The MB probe dye was degraded under UV irradiation adding 0.5 mL of hydrogen peroxide solution (50 wt% in H_2O, Aldrich) in 5 mL of microblock dispersed water.

FEM Analysis: The conventional FEM software (COMSOL Multiphysics v. 5.6, Structural Mechanics Module, physics-controlled mesh (basic auto mesh)) was used to simulate the deformed shapes of the wet TiO_2 paste after shrinkage. The structure was designed in a 3D shape by using 3D Max and imported into COMSOL. The isotropic solid model of a linear elastic material in the solid mechanics module was used in the physics. We applied a strain of −20% to pyramid structures consisting of the wet TiO_2 paste and fixed inside the structures patterned by square shapes consisting of solidified TiO_2. The Poisson's ratio and Young's modulus of the wet TiO_2 paste material properties were set to 0.27 and 288 GPa, respectively. The geometry of the structures was the same as our pattern.

Image Analysis for Anti-Counterfeiting Functions: Image Processing ToolboxTM (version 11.6) in MATLAB (R2022b, version 9.13) was utilized to decode the anti-counterfeiting films through measuring rotation angles of the microblocks. Microblocks were detected as "Connected Components" from the image, and binarization and edge detection processes were followed in order. The center coordinates and side lengths of the microblocks were estimated by averaging indices and the number of the foreground pixels, respectively. To estimate the rotation angles precisely, the distance from the points at each edge to the center was listed in sequence. The minimum values and the maximum values corresponded to distances to the mid-point of each side and distances to each vertex respectively, which can be utilized for calculating rotation angles through vectorization indices of these values. As a result, the fitted squares for the microblocks could be detected, as shown in Figure S10 (Supporting Information). Concentric circles enabled to sort dent or cambered microblocks, which determined whether only pixels near vertexes or the pixels near mid-points were utilized. Through this pre-processing, this method also worked effectively in the case of microblocks with defects.

Characterization: SEM and EDS analysis were performed with a field-emission scanning electron microscope (JSM-6701F, JEOL) at an accelerating voltage of 10.0 kV. Confocal microscopy was performed under 405, 561, and 640 nm lasers (Super Sensitive CLSM, Zeiss). Fluorescence microscopy images were obtained by KI-200F. The zeta potential of charged microblocks was measured by an electrophoretic light scattering spectrophotometer (ELS-8000).

Supporting Information

Supporting Information is available from the Wiley Online Library or from the author.

Acknowledgements

This work was supported by Basic Science Research Program through the National Research Foundation of Korea (NRF) funded by the Ministry of Education (NRF-2021R1A6A1A03039981 and NRF-2020R1A2C1011571), and the National Creative Research Initiative Program for "Intelligent Hybrids Research Center" (no. 2010–0018290) funded by a National Research Foundation of Korea (NRF) grant.

Conflict of Interest

The authors declare no conflict of interest.

Data Availability Statement

The data that support the findings of this study are available from the corresponding author upon reasonable request.

Keywords

colloids, cracks, mesoporous particles, microblocks, separation

Received: January 31, 2023
Revised: April 18, 2023
Published online:

[1] S. C. Glotzer, M. J. Solomon, *Nat. Mater.* **2007**, *6*, 557.
[2] Y. Xia, T. D. Nguyen, M. Yang, B. Lee, A. Santos, P. Podsiadlo, Z. Tang, S. C. Glotzer, N. A. Kotov, *Nat. Nanotechnol.* **2011**, *6*, 580.
[3] T. Wang, D. LaMontagne, J. Lynch, J. Q. Zhuang, Y. C. Cao, *Chem. Soc. Rev.* **2013**, *42*, 2804.
[4] S. Wintzheimer, T. Granath, M. Oppmann, T. Kister, T. Thai, T. Kraus, N. Vogel, K. Mandel, *ACS Nano* **2018**, *12*, 5093.
[5] M. S. Mauter, I. Zucker, F. Perreault, J. R. Werber, J.-H. Kim, M. Elimelech, *Nat. Sustainability* **2018**, *1*, 166.
[6] S. Wintzheimer, J. Reichstein, P. Groppe, A. Wolf, B. Fett, H. Zhou, R. Pujales-Paradela, F. Miller, S. Müssig, S. Wenderoth, K. Mandel, *Adv. Funct. Mater.* **2021**, *31*, 2011089.
[7] S. Li, J. Liu, N. S. Ramesar, H. Heinz, L. G. Xu, C. L. Xu, N. A. Kotov, *Nat. Commun.* **2019**, *10*, 4826.
[8] K. Hou, J. Han, Z. Tang, *ACS Mater. Lett.* **2020**, *2*, 95.
[9] X. Guo, N. Xue, M. Zhang, R. Ettelaie, H. Yang, *Nat. Commun.* **2022**, *13*, 5953.
[10] Q. Zhang, T. P. Chou, B. Russo, S. A. Jenekhe, G. Cao, *Adv. Funct. Mater.* **2008**, *18*, 1654.
[11] W. Wu, J. Yuan, S. Dong, J. Hao, *ACS Cent. Sci.* **2021**, *7*, 1611.
[12] Z. X. Wu, D. Y. Zhao, *Chem. Commun.* **2011**, *47*, 3332.
[13] D. W. Lee, M. H. Jin, C. B. Lee, D. Oh, S. K. Ryi, J. S. Park, J. S. Bae, Y. J. Lee, S. J. Park, Y. C. Choi, *Nanoscale* **2014**, *6*, 3483.
[14] J. Liu, H. Chu, H. Wei, H. Zhu, G. Wang, J. Zhu, J. He, *RSC Adv.* **2016**, *6*, 50061.
[15] H. Canziani, B. Hanschmann, F. Tischer, A. Sommereyns, T. Distler, J. Schramm, N. Hesse, J. Schmidt, A. Grünewald, R. Detsch, A. Boccaccini, M. Maskos, M. Schmidt, N. Vogel, *Adv. Funct. Mater.* **2022**, *32*, 2205730.
[16] J. Reichstein, F. Miller, S. Wintzheimer, K. Mandel, *Adv. Funct. Mater.* **2021**, *31*, 2104189.
[17] S. Müssig, J. Reichstein, F. Miller, K. Mandel, *Small* **2022**, *18*, 2107511.
[18] J. Reichstein, S. Müssig, H. Bauer, S. Wintzheimer, K. Mandel, *Adv. Mater.* **2022**, *34*, 2202683.
[19] H. Zhou, R. P-Paradela, P. Groppe, S. Wintzheimer, K. Mandel, *Part. Part. Syst. Charact.* **2022**, *39*, 2200127.
[20] G. Guo, L. Ji, X. Shen, B. Wang, H. Li, J. Hu, D. Yang, A. Dong, *J. Mater. Chem. A* **2016**, *4*, 16128.
[21] J. Wang, E. Kang, U. Sultan, B. Merle, A. Inayat, B. Graczykowski, G. Fytas, N. Vogel, *J. Phys. Chem. C* **2021**, *125*, 23445.
[22] Z. Yu, C. F. Wang, L. Ling, L. Chen, S. Chen, *Angew. Chem., Int. Ed.* **2012**, *51*, 2375.
[23] M. A. Sahin, H. Werner, S. Udani, D. D. Carlo, G. Destgeer, *Lab Chip* **2022**, *22*, 4007.
[24] S. Wooh, H. Huesmann, M. N. Tahir, M. Paven, K. Wichmann, D. Vollmer, W. Tremel, P. Papadopoulos, H.-J. Butt, *Adv. Mater.* **2015**, *27*, 7338.
[25] H. Tan, S. Wooh, H.-J. Butt, X. Zhang, D. Lohse, *Nat. Commun.* **2019**, *10*, 478.
[26] W. Liu, M. Kappl, W. Steffen, H.-J. Butt, *J. Colloid Interface Sci.* **2022**, *607*, 1661.
[27] J. Kim, H. Hwang, H.-J. Butt, S. Wooh, *J. Colloid Interface Sci.* **2021**, *588*, 157.

[28] S. Wooh, S. Lee, Y. Lee, J. H. Ryu, W. B. Lee, H. Yoon, K. Char, *ACS Nano* **2016**, *10*, 9259.
[29] L. Guo, Y. Ren, L. Y. Kong, W. K. Chim, S. Y. Chiam, *Nat. Commun.* **2016**, *7*, 13148.
[30] X. Ma, J. Lowensohn, J. C. Burton, *Phys. Rev. E* **2019**, *99*, 012802.
[31] Y. Lee, J. Kim, S. Lee, S. Wooh, H. Yoon, K. Char, *Langmuir* **2022**, *38*, 4935.
[32] J. J. Kim, K. W. Bong, E. Reategui, D. Irimia, P. S. Doyle, *Nat. Mater.* **2017**, *16*, 139.
[33] W. Sun, F. Jia, Z. Sun, J. Zhang, Y. Li, X. Zhang, B. Yang, *Langmuir* **2011**, *27*, 8018.